

Entropy-driven multiscale defects enhance the thermoelectric properties of ZrCoSb-based half-Heusler alloys

Rongchun Chen^a, Quanwei Jiang^a, Lifeng Jiang^a, Ruonan Min^a, Huijun Kang^{a,b,*},
Zongning Chen^{a,b}, Enyu Guo^{a,b}, Xiong Yang^a, Tongmin Wang^{a,b,*}

^a Key Laboratory of Solidification Control and Digital Preparation Technology (Liaoning Province), School of Materials Science and Engineering, Dalian University of Technology, Dalian 116024, China

^b Ningbo Institute of Dalian University of Technology, Ningbo 315000, China

ARTICLE INFO

Keywords:

Thermoelectric properties
Entropy engineering
Half-Heusler alloy
Low thermal conductivity

ABSTRACT

As a new method of alloying, entropy engineering has proven to be an effective strategy to decrease the lattice thermal conductivity (κ_L). However, the majority of entropy engineering applications of half-Heusler alloys (HHs) are suboptimal. The poor Seebeck coefficients (S) and obscure underlying electron and phonon transport mechanisms of medium- and high-entropy HHs hinder the further optimization of their thermoelectric properties. Herein, a systematic synthesis of *n*-type ZrCoSb-based medium-entropy HHs is reported, along with a corresponding structural, theoretical, and thermoelectric study. It is demonstrated that the effectively decreased κ_L in medium-entropy HHs was mainly due to the scattering of atomic disorder, in addition to the vacancies, stacking faults, dislocations, and nano-domains/precipitates. Using density functional theory calculations, we attribute the lower S to the lower density-of-states (DOS) effective mass and the slowly changing DOS at Fermi level. By optimizing the spark plasma sintering temperature, an ultralow κ_L of 1.27 W m⁻¹ K⁻¹ was achieved in the Zr_{0.6}(NbTa)_{0.4}CoSb medium-entropy HH alloy at 923 K. In conjunction with the improved power factor, the highest peak figure-of-merit value of ~0.42 was achieved for the Zr_{0.6}(NbTa)_{0.4}CoSb medium-entropy HH alloy. This study provides a guidance for the design and further optimization of the thermoelectric properties for medium-entropy HH alloys.

1. Introduction

Thermoelectric (TE) materials can convert waste heat into useful electrical energy and have demonstrated a promising role in the achievement of carbon neutrality [1,2]. The evaluation criteria for TE materials are based on the dimensionless figure-of-merit (ZT), which is defined as $S^2\sigma T/\kappa$, where S is the Seebeck coefficient, σ is the electrical conductivity, κ is the thermal conductivity, and T is the absolute temperature. Half-Heusler alloys (HHs) are among the state-of-the-art TE materials owing to their robust mechanical properties and excellent thermal stabilities [3–6]. However, the high lattice thermal conductivities (κ_L) of these HHs hinder any further improvement in their TE properties.

The most recent studies aimed at reducing the κ of HHs have focused on alloying, nano-structuring, and phase separation [7–10]. In addition, as a new alloying method, the concept of entropy engineering has

proven to be an effective strategy to reduce κ in other types of TE materials [11–18]. For example, Jiang et al. synthesized a series of TE materials with ultrahigh TE properties through entropy engineering, including the high-entropy Pb_{0.975}Na_{0.025}Se_{0.5}S_{0.25}Te_{0.25}, which exhibited a high ZT_{max} of ~2.0 at 900 K, and possessed band convergence as well as hierarchical structures [11]. In terms of germanium telluride-based high-entropy materials, the value of ZT_{max} was enhanced to 2.7 at 750 K by tuning the localization of electrons and phonons [12]. Moreover, in an *n*-type PbSe-based high-entropy material, the value of ZT_{max} reached 1.8 at 900 K through entropy-driven structural stabilization owing to the presence of largely distorted lattices [13]. Similarly, Wang et al. reported that the κ of medium-entropy Si_yGe_ySn_x alloys decreased with an increasing compositional disorder owing to enhanced Anderson localization and the presence of strong phonon-phonon anharmonic interactions [19]. Additionally, Zhao et al. highlighted the importance of entropy engineering in terms of the TE performance and

* Corresponding authors at: Key Laboratory of Solidification Control and Digital Preparation Technology (Liaoning Province), School of Materials Science and Engineering, Dalian University of Technology, Dalian 116024, China.

E-mail addresses: kanghuijun@dlut.edu.cn (H. Kang), tmwang@dlut.edu.cn (T. Wang).

phase stability, which benefited to the intrinsically low lattice thermal conductivity (κ_L) and well-maintained carrier mobility (μ); a peak ZT value of ~ 0.86 was attained at 790 K for cubic $\text{AgBi}_{0.8}\text{Sb}_{0.2}\text{Se}_2$ after bromine doping [20]. These studies therefore demonstrate that the configurational entropy is an effective descriptor in the materials genome approach for developing high performance TE materials. It has also been reported that the introduction of extensive alloying/point defects (i.e., site and size disorders) increases the configurational entropy and decreases the κ_L of the system simultaneously. For example, a low κ_L of $2.5 \text{ W m}^{-1} \text{ K}^{-1}$ and a high ZT_{\max} of ~ 0.88 were achieved in $\text{Nb}_{1-x}\text{M}_x\text{FeSb}$ ($\text{M} = \text{Hf, Zr, Mo, V, Ti}$; equimolar) high-entropy HHs at 873 K through the introduction of high-entropy effects [21]. However, it should be emphasized that a high configurational entropy itself does not ensure a high value of ZT_{\max} , since low S and ZT_{\max} values are often the result of entropy engineering for the prepared HHs. For example, undesirable ZT_{\max} values of ~ 0.3 and ~ 0.25 were obtained for high-entropy n -type MCoSb and p -type $\text{MFe}_{0.6}\text{Co}_{0.4}\text{Sb}$ ($\text{M} = \text{Ti, Zr, Hf, V, Nb, and Ta}$) HHs, respectively [22]. Similarly, a low ZT_{\max} value of ~ 0.13 was achieved at 973 K for the $\text{Ti}_2\text{NiCoSnSb}$ high-entropy HH alloy [23]. Compared with other medium- and high-entropy TE materials, the lower S is rationale for the poor ZT_{\max} values that are generally obtained for HHs. However, the corresponding band structures have rarely been evaluated or employed to explain these poor S . Moreover, the ultralow κ_L is often attributed to the contribution of entropy-driven atomic disorder and the localization of electrons and phonons. The phonon transport mechanisms for medium-entropy HHs containing precipitation particles must therefore be further clarified in detail relative to other medium- and high-entropy TE materials.

Thus, we herein report the tuning of the configurational entropy and compositional disorder degree of $\text{Zr}_{1-x}(\text{NbTa})_x\text{CoSb}$ ($x = 0, 0.1, 0.15, 0.2, 0.25, 0.3, 0.35, \text{ and } 0.4$) HHs by varying the contents of Nb and Ta from 0 to 0.4. Subsequently, the corresponding band structures of the medium-entropy HHs with lower S are revealed by means of density functional theory (DFT) calculations, and the phonon transport mechanisms are investigated using scanning transmission electron microscopy (STEM) and in situ Raman spectroscopy. Overall, we aim to demonstrate an in-depth understanding of the TE transport mechanisms of medium-entropy HHs and to provide guidance for further optimization of the TE properties for medium-entropy HHs and other medium-entropy TE systems.

2. Experimental details

High-purity Zr (99.5 %), Nb (99.99 %), Ta (99.99 %), Co (99.95 %), and Sb (99.99 %) were weighed according to the nominal stoichiometric ratios of the desired $\text{Zr}_{1-x}(\text{NbTa})_x\text{CoSb}$ species ($x = 0, 0.1, 0.15, 0.2, 0.25, 0.3, 0.35, \text{ and } 0.40$). Ingots of $\text{Zr}_{1-x}(\text{NbTa})_x\text{CoSb}$ HHs were prepared by levitation melting (LMF, FM-40, Kejing, China), and the broken ingots were ball-milled in a planetary ball mill machine (Pulverisette 4, Fritsch, Germany). The ball-milled powders were then sintered at 1173 K for 2 min at a pressure of 50 MPa in a spark plasma sintering (SPS) furnace (SPS, SPS-30, Chen Hua, China). To further optimize the electrical properties, additional sintering temperatures (1123, 1223, 1273, and 1323 K) were also evaluated.

The phase components of the HHs were examined using XRD (Empyrean, PANalytical, Netherlands). STEM samples were prepared using a dual-beam focused ion beam (FIB, LYRA3 FIB-SEM, TESCAN, Czech Republic). Atomic resolution HAADF imaging was performed using a probe-corrected STEM (FEI Titan G2 60–300, FEI, USA) equipped with a cold-field emission source. The atomic stress distribution was analyzed using Strain++ software. The active Raman vibration modes were identified by Raman spectroscopy (inVia Qontor, Renishaw, UK) between 100 and 298 K using a solid-state argon laser at $\lambda = 532 \text{ nm}$, and with a spectral resolution of $\sim 1 \text{ cm}^{-1}$. The σ and S were simultaneously measured using a commercial instrument (LSR-3, Linseis, Germany) at temperatures between 323 and 923 K. The corresponding thermal

diffusivity, specific heat capacity (C_p), and density were measured using the flash diffusivity method (LFA457, Netzsch, Germany), differential scanning calorimetry (404 F3, Netzsch, Germany), and the Archimedes method, respectively. The Hall coefficient was measured at room temperature using a commercial Lake Shore 8400 instrument (Lake Shore, US) with a measurement uncertainty of $\pm 10 \%$. The corresponding n and μ were then calculated using the obtained Hall coefficient. The sound velocity was measured using a Panametrics 5052 pulser/receiver with a 0.03 MHz filter. The responses were recorded using a Tektronix TDS5054B-NV digital oscilloscope. The accuracies of the S , σ , and κ measurements were ± 5 , ± 3 , and $\pm 7 \%$, respectively.

All DFT calculations were performed using the Vienna ab initio simulation package (VASP) [24,25] with the projector augmented-wave [26] potential and the Perdew–Burke–Ernzerhof form for the generalized gradient approximation (GGA) for the exchange–correlation functional [27]. A 60-atom $5 \times 1 \times 1$ supercell of ZrCoSb was built to calculate the band structure with Nb and Ta co-doping. The energy cut-off of the plane-wave basis, the convergence of the total energy, and the force were set to 400 eV, 1×10^{-6} eV, and $0.03 \text{ eV } \text{\AA}^{-1}$, respectively. The Brillouin zone was sampled using a Monkhorst–Pack k-point grid with a uniform spacing of 0.03 \AA^{-1} . Band unfolding was calculated using the KPROJ program, based on the k-projection method [28–30].

3. Results and discussion

3.1. Structural characterization

Fig. 1(a) shows the room-temperature X-ray powder diffraction (XRD) patterns recorded for the sintered $\text{Zr}_{1-x}(\text{NbTa})_x\text{CoSb}$ ($x = 0, 0.1, 0.15, 0.2, 0.25, 0.3, 0.35, \text{ and } 0.4$) HHs. As shown in this figure, the diffraction peaks match well with those of ZrCoSb (PDF#54–0448), which possesses a cubic MgAgAs-type structure. In addition, some small peaks corresponding to the presence of precipitates are also present. It is clear that the diffraction peaks gradually shift to a larger degree upon increasing x , and peak splitting can be observed when $x > 0.25$, indicating that the split peak corresponds to an ordered HHs phase with a similar lattice parameter. As summarized in **Fig. 1(b)**, we calculated the lattice parameters and configurational entropies for the various prepared HHs, wherein the configurational entropy of a given system can be calculated using Eq. (1) [22]:

$$\Delta S_{\text{mix}} = -R \left[\left(\sum_{h=1}^M x_h \ln x_h \right)_{x-\text{site}} + \left(\sum_{i=1}^N x_i \ln x_i \right)_{y-\text{site}} + \left(\sum_{j=1}^L x_j \ln x_j \right)_{z-\text{site}} \right] \quad (1)$$

where R is the gas constant; M , N , and L are the numbers of the constituent elements at the X , Y , and Z sites, respectively; and x_h , x_i , and x_j are the mole fractions of the elements at the X , Y , and Z sites, respectively. In general, the calculated value of the configurational entropy is $0.69 R < \Delta S_{\text{mix}} < 1.5 R$, which corresponds to a medium-entropy alloy. It was found that upon increasing the doping content (i.e., the value of x), the lattice constants gradually decreased while the configurational entropy gradually increased. Surprisingly, peak splitting was observed only in the medium-entropy HHs.

Fig. 2 shows low-magnification images and the corresponding elemental mapping images recorded for the HH microstructures. As shown in **Fig. 2(a)–(c)**, the backscattered electron (BSE) microscopy results indicate that no obvious pores were present in the $\text{Zr}_{1-x}(\text{NbTa})_x\text{CoSb}$ ($x = 0, 0.1, \text{ and } 0.4$) HHs, and the grain size remained relatively constant among these samples. Remarkably, some distinct precipitates were found to be distributed along the grain boundaries within the Nb and Ta co-doped HHs, and the number of precipitates increased upon increasing the doping content. To further understand the precipitates along the grain boundaries, high-angle annular dark field (HAADF)-STEM was carried out for the $\text{Zr}_{0.6}(\text{NbTa})_{0.4}\text{CoSb}$ medium-

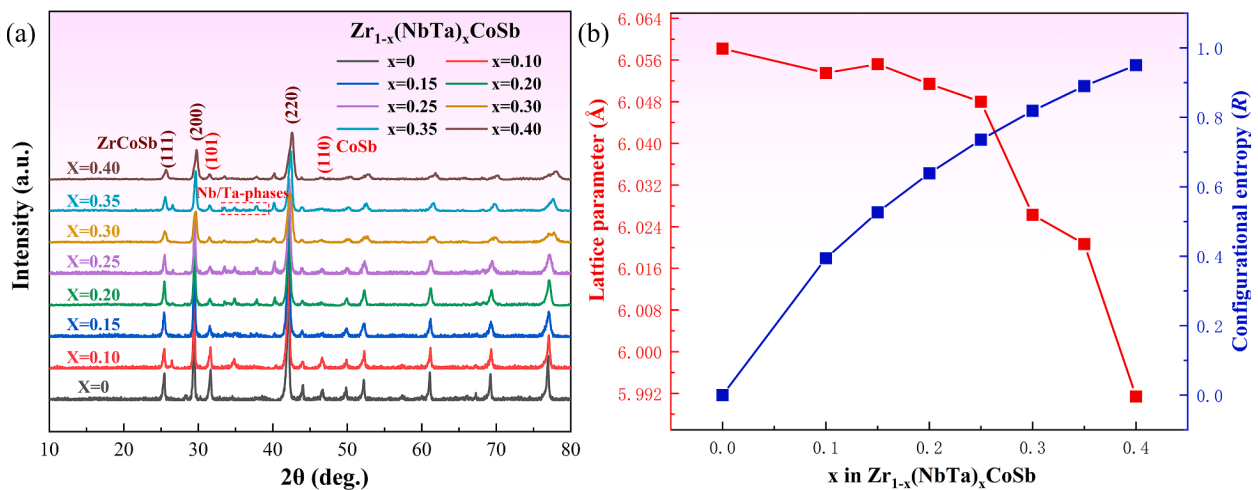


Fig. 1. (a) XRD patterns for $Zr_{1-x}(NbTa)_xCoSb$ ($x = 0, 0.1, 0.15, 0.2, 0.25, 0.3, 0.35$, and 0.4). (b) Calculated lattice constants according to the recorded diffraction peaks, and the corresponding configurational entropies.

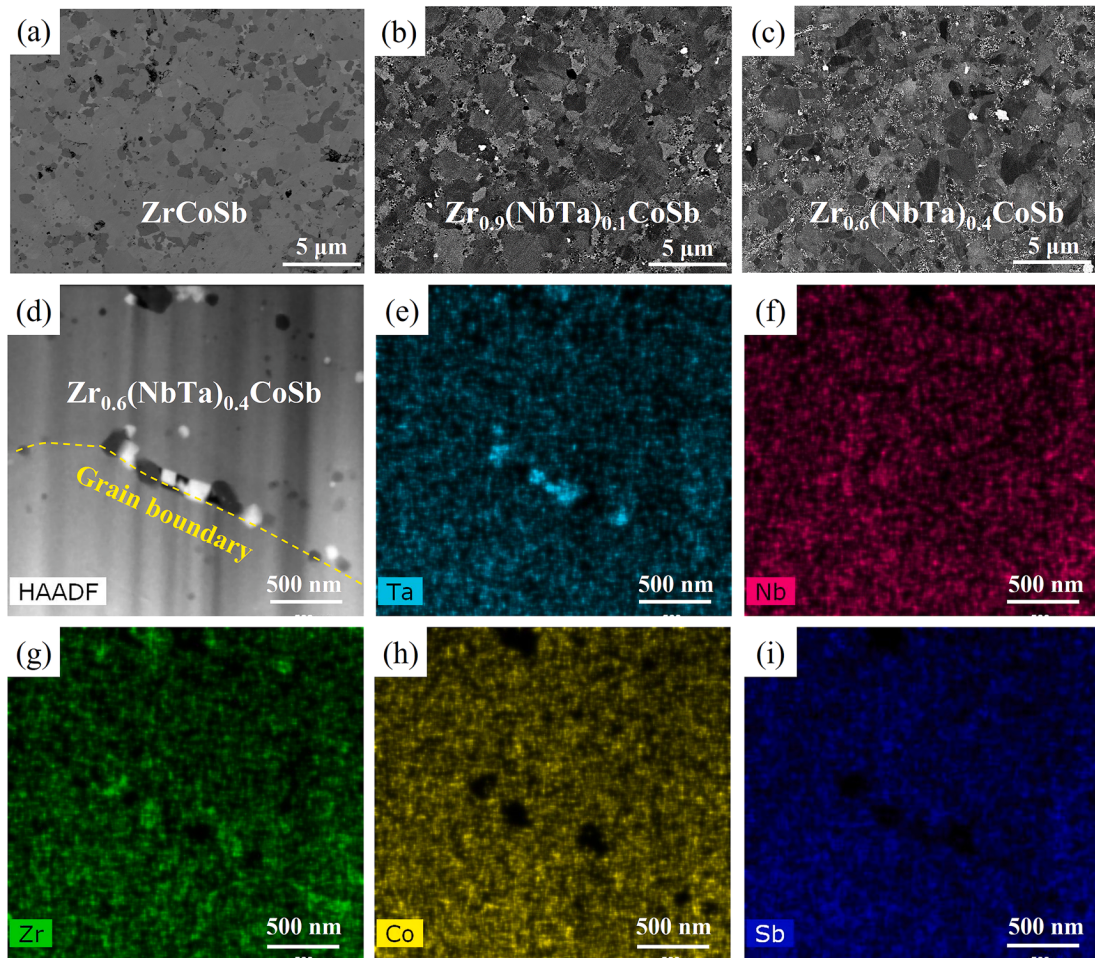


Fig. 2. BSE images for the (a) ZrCoSb, (b) $Zr_{0.9}(NbTa)_{0.1}CoSb$, and (c) $Zr_{0.6}(NbTa)_{0.4}CoSb$ HHs. (d) HAADF-STEM image for $Zr_{0.6}(NbTa)_{0.4}CoSb$ and (e)–(i) the corresponding elemental mapping images for Ta, Nb, Zr, Co, and Sb, respectively.

entropy HH alloy. As shown in Fig. 2(d)–(i), all examined elements were homogeneously distributed within the matrix, and the bright white and black precipitates can be identified as Ta-enriched and Zr- and Nb-enriched precipitates, respectively, which are able to effectively scatter medium-frequency phonons. Meanwhile, numerous nanoprecipitates can be seen in the grain interiors; the corresponding

phonon transport mechanisms for these precipitates are discussed in Section 3.4.1.

3.2. TE properties

Fig. 3 shows the temperature-dependent TE properties of the

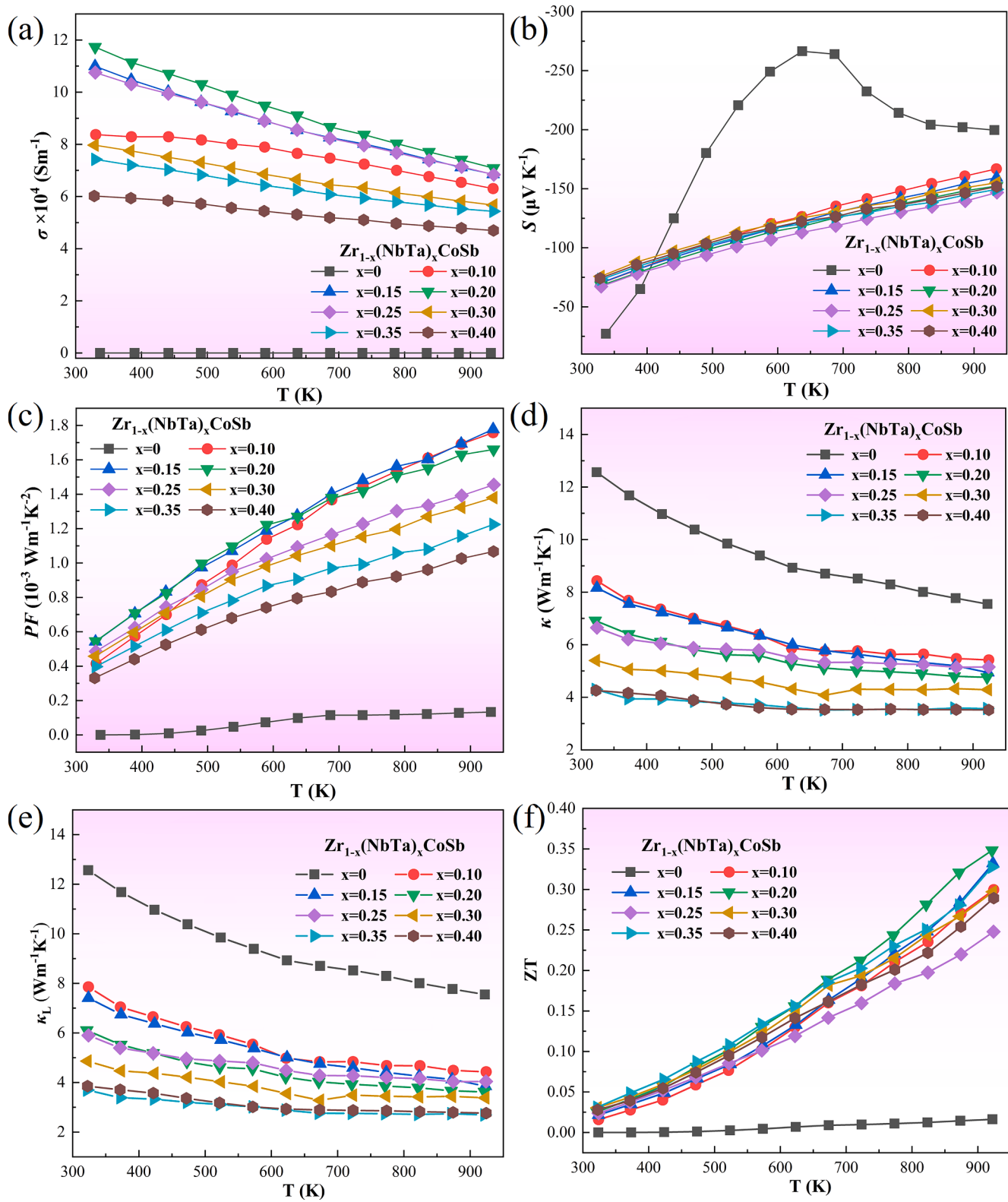


Fig. 3. Temperature dependences of (a) σ , (b) S , (c) PF , (d) κ , (e) κ_L , and (f) ZT in the $Zr_{1-x}(NbTa)_xCoSb$ HHs.

$Zr_{1-x}(NbTa)_xCoSb$ ($x = 0, 0.1, 0.15, 0.2, 0.25, 0.3, 0.35$, and 0.4) HHs. More specifically, as shown in Fig. 3(a), the pristine $ZrCoSb$ HH alloy exhibited an ultralow electrical conductivity (σ) over the entire temperature range, while all Nb and Ta co-doped HHs showed the enhanced σ . Upon increasing the Nb and Ta doping contents, the σ initially increased and then decreased at the same temperature, and the

maximum σ was obtained for the $Zr_{0.8}(NbTa)_{0.2}CoSb$ HH alloy; this enhancement in σ is mainly due to the doping-induced enhanced carrier concentration (n) [31,32]. Combined with the results shown in Figs. 1 and 2, the decrease in σ for the $Zr_{1-x}(NbTa)_xCoSb$ ($x > 0.2$) HHs can be mainly attributed to the increasing degrees of entropy-driven atomic disorder and carrier scattering. In addition, The S of all HHs is negative,

indicating a typical electron-type transport behavior, as shown in Fig. 3(b). For the Nb and Ta co-doped HHs, the absolute value of S increased gradually upon increasing the temperature, and no intrinsic excitation occurred. As shown in Fig. 3(c), benefiting from the enhanced σ , the power factor ($PF = S^2\sigma$) of $Zr_{0.85}(NbTa)_{0.15}CoSb$ was significantly improved over the entire temperature range, and PF_{max} was enhanced from $0.13 \times 10^{-3} \text{ W cm}^{-1} \text{ K}^{-2}$ for the pristine $ZrCoSb$ to $1.8 \times 10^{-3} \text{ W cm}^{-1} \text{ K}^{-2}$ for $Zr_{0.85}(NbTa)_{0.15}CoSb$ at 923 K.

As expected, in terms of the high κ of the $ZrCoSb$ HH alloy, an increased entropy is an alternative option to further decrease the κ_L and thereby the corresponding κ (Fig. 3(d) and (e)). As previously reported, κ_L is calculated by subtracting the electronic contribution ($\kappa_e = L\sigma T$)

from κ , with the Lorenz factor (L) being determined by the single parabolic band model [33,34]. As shown in Fig. 3(d) and (e), a gradual saturation is observed for the phonon scattering upon increasing the doping content from 0.10 to 0.40. More specifically, the κ_L of the $ZrCoSb$ HH alloy decreased by 62.7 %, i.e., from $7.5 \text{ W m}^{-1} \text{ K}^{-1}$ for the pristine $ZrCoSb$ to $2.8 \text{ W m}^{-1} \text{ K}^{-1}$ for $Zr_{0.60}(NbTa)_{0.40}CoSb$ at 923 K. The κ_L is close to that of $Nb_{0.8}Hf_{0.2}FeSb_{0.88}Sn_{0.12}$ [35] and lower than that of other reported HHs, such as $ZrFe_{0.2}Co_{0.8}Sb$ [36], $Zr_{0.25}Hf_{0.75}Ni_{1.03}Sn_{0.975}Sb_{0.025}$ [37], and 1.5 % InSb-TiCo_{0.85}Fe_{0.15}Sb [38]. Fig. 3(f) plots the value of ZT as a function of temperature for the $Zr_{1-x}(NbTa)_xCoSb$ HHs. Based on the synergistically optimized electrical and thermal properties, a ZT_{max} of ~ 0.35 was achieved for the

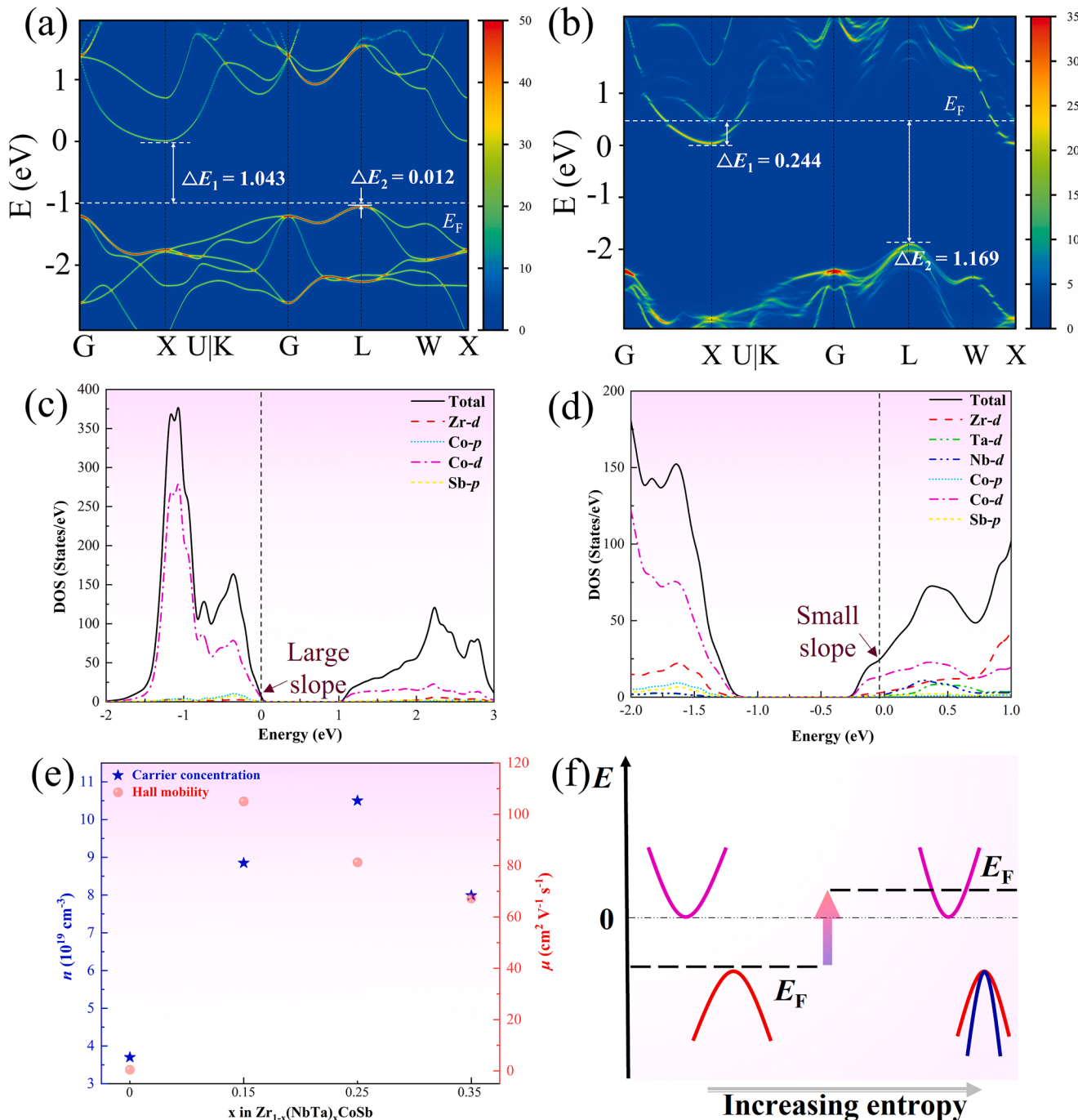


Fig. 4. Band structures and corresponding DOS of the HHs: (a) and (c) $Zr_{20}Co_{20}Sb_{20}$, (b) and (d) $Zr_{18}Nb_1Ta_1Co_{20}Sb_{20}$. (e) The n and μ for samples containing different amounts of the Nb and Ta dopants. (f) Schematic diagram representing the evolution of the band structure with an increase in the entropy.

$\text{Zr}_{0.80}(\text{NbTa})_{0.20}\text{CoSb}$ HH alloy at 923 K, which is close to that of $\text{Ti}(\text{Fe}_{1-x}\text{Co}_{1/3}\text{Ni}_{1/3-x}\text{Sb})$ at 923 K [39].

3.3. Electronic transport mechanism

Although a ZT_{\max} of ~ 0.35 was obtained for the $\text{Zr}_{0.85}(\text{NbTa})_{0.15}\text{CoSb}$ HH alloy at 923 K, the value is significantly lower than that of the Nb/Ta singly-doped ZrCoSb-based HHs. For example, $\text{Zr}_{0.88}\text{Nb}_{0.12}\text{CoSb}$ and $\text{Zr}_{0.86}\text{Ta}_{0.14}\text{CoSb}$ demonstrated peak ZT values of ~ 0.5 and ~ 0.7 at 923 K, respectively [40], which can be ascribed to a high PF_{\max} of $> 2.8 \times 10^{-3} \text{ W m}^{-1} \text{ K}^{-2}$. However, the highest PF_{\max} achieved for the various $\text{Zr}_{1-x}(\text{NbTa})_x\text{CoSb}$ HH alloys was only $1.8 \times 10^{-3} \text{ W m}^{-1} \text{ K}^{-2}$ at the same temperature. Theoretically, the reduction of S in single-doped HHs can be mainly ascribed to the increased n . However, for the same value of σ , the S of the $\text{Zr}_{1-x}(\text{NbTa})_x\text{CoSb}$ HHs decreased by $\sim 50\%$ compared with that of the singly-doped counterpart. For the Nb and Ta co-doped HHs, it is not suitable to explain the serious reduction of S only from the perspective of n . To reveal the cause of these poor S values, we calculated the band structure and corresponding density-of-states (DOS) for the $\text{Zr}_{0.9}(\text{NbTa})_{0.1}\text{CoSb}$ HH alloy. As shown in Fig. 4(a), taking the conduction band minimum as a standard, the valence band maximum is 0.012 eV lower than the Fermi level (E_F) for pristine ZrCoSb alloy. With the Nb and Ta co-doping, the E_F crossed to the conduction band, which is 0.244 eV higher than the conduction band minimum. It provides more conduction channels for charge carriers and thus results in a higher σ and lower S . Similar to the singly-Nb/Ta-doped HH alloys [40], no defect states were observed in the band gap of the $\text{Zr}_{0.9}(\text{NbTa})_{0.1}\text{CoSb}$ HH alloy. Although there is a slight difference in the band gap between the pristine ZrCoSb and $\text{Zr}_{0.9}(\text{NbTa})_{0.1}\text{CoSb}$ HH alloys, the energy required for the electronic transition of the latter increases, thereby suppressing the intrinsic excitation.

In addition, the roles of entropy engineering in promoting band degeneracy and multivalley characteristic have also been reported for other TE systems [11,12]. Unfortunately, entropy-driven band convergence and multivalley were introduced into valence bands instead of conduction bands in n -type $\text{Zr}_{0.9}(\text{NbTa})_{0.1}\text{CoSb}$ HH alloy. Theoretically, entropy-driven band engineering is more suitable for p -type ZrCoSb-based HHs. As shown in Fig. 4(c) and (d), Nb and Ta co-doping decreased the total DOS peak and resulted in a smaller slope at E_F . Based on the Boltzmann transport theory, a slowly changing DOS at E_F is expected to a lower S [41]. Therefore, the changing of DOS at E_F is partly accounted for the poor S and PF_{\max} .

To further clarify the origin of the poor S , the room-temperature n and μ were analyzed. As shown in Fig. 4(e), upon increasing x in the $\text{Zr}_{1-x}(\text{NbTa})_x\text{CoSb}$ HH, n initially increases and then decreases, and the maximum n reaches $10.5 \times 10^{19} \text{ cm}^{-3}$ in the $\text{Zr}_{0.75}(\text{NbTa})_{0.25}\text{CoSb}$ HH alloy. When the doping content was > 0.25 , n and μ began to decrease due to the donor doping elements existing as precipitates (Fig. 2(c)) and the increased degree of carrier scattering. Based on these results, the corresponding evolution mechanisms of σ and S became clear. However, the poor S recorded for the medium-entropy HHs is disproportionate to the change in n , and it was reasonable to infer that an underlying and unknown contribution may also exist. Generally, the single band effective mass (m_b^*) is known to be an intrinsic physical quantity that is inversely proportional to the curvature of the band for a TE material. For a degenerate semiconductor, the S is proportional to the DOS effective mass m_d^* , $m_d^* = N_v^{2/3} m_b^*$, where N_v is the valley degeneracy [33]. Therefore, a narrower band leads to a smaller m_b^* , m_d^* and S . As shown in Fig. 4(f), the valence bands were relatively narrow after Nb and Ta co-doping. Although the reduction of the m_b^* is beneficial in terms of improving μ , it also leads to a drastic reduction of m_d^* and S in the medium-entropy HHs. Overall, it appears that optimizing the type of doping element to increase the slope of DOS at E_F and the m_d^* may be key to regulate the electrical properties of $\text{Zr}_{1-x}(\text{NbTa})_x\text{CoSb}$ medium-

entropy HHs.

3.4. Phonon transport mechanisms

3.4.1. Multiscale defects

To gain an improved understanding of the relationship between the structural characteristics and the remarkably low κ_L of the prepared HH alloys, the precipitates present in the alloys were further investigated by HAADF-STEM. Fig. 5(a) shows the Nb-, Ta-, and Zr-enriched nano-domains that are locally inserted in the matrix, and the formation of these nano-domains can be attributed to the locally off-stoichiometric ratios of TE materials, such as the ZrNiSn-based HH alloy [42]. However, these nano-domains have rarely been reported for ZrCoSb-based HHs. It is therefore reasonable to infer that the nano-domains present in the current system mainly originated from the locally strong inner stress and delayed diffusion effect introduced by entropy engineering. In this context, Yang et al. verified that although these nano-domain boundaries generally possess weaker interface features and stress field fluctuations in the lattices than those of the precipitates and grain boundaries, they can still be considered as scattering centers for phonons [43]. In addition, bright white Ta-enriched spherical precipitates with sizes of $\sim 15\text{--}40$ nm were clearly observed in the matrix, as can be seen in Fig. 5(b) and (c). Furthermore, the Nb atoms present in the matrix exist in the form of nano-precipitates. As shown in Fig. 5(d) and (e), Nb- and Zr-enriched nano-spherical and Nb- and Ta-enriched nano-hexagonal precipitates were also observed in the matrix, while a portion of the Ta atoms (see Fig. 5(f)) are present in the form of nano-domains, inserting into the nano-hexagonal precipitates. Consequently, these nano-domains, nano-spherical precipitates, and nano-hexagonal precipitates result in a strong scattering of phonons to effectively reduce the κ_L in multiscale locally off-stoichiometric medium-entropy HHs.

As shown in Fig. 6(a) and (b), some vacancies were observed in the HAADF-STEM image of the $\text{Zr}_{0.6}(\text{NbTa})_{0.4}\text{CoSb}$ HH alloy, including the typical Co-interstitial defects formed through the swapping of Co atoms with the structural vacancies of the HH structure. It should be noted here that a similar result (i.e., the presence of Ni-interstitial defects in ZrNiSn-based HH alloys) was reported in our previous work [44]. In addition, the line intensity profiles of the individual atomic columns (Fig. 6(c)) clearly confirm the Co-interstitial defects, which lead to an increasing degree of atomic disorder. This, in turn, can effectively scatter phonons and simultaneously reduce the κ_L . Generally, the presence of incoherent phase interfaces indicates a larger lattice misfit and can induce a stress field fluctuation to scatter phonons [45]. However, coherent phase interfaces are usually neglected, especially in the context of nano-precipitates. As shown in Fig. 6(d)–(f), lattice defects, such as dislocations, can be frequently observed at the coherent phase interfaces between the nano-precipitates and the matrix. Since dislocations can often reflect the spatially varying strains that inhibit the transportation of phonons at coherent interfaces, the obtained results indicate that the lattice distortion observed at the coherent interface between the Ta-enriched precipitates and the matrix can lead to the scattering of phonons and reduce the κ_L for the $\text{Zr}_{0.6}(\text{NbTa})_{0.4}\text{CoSb}$ medium-entropy HH alloy. Remarkably, taking the Nb- and Zr-enriched nano-spherical precipitates as an example, the geometric phase analysis (GPA) results presented in Fig. 6(h) and 6(i) show that a more significant stress field fluctuation is observed in the precipitates, except at the coherent interface. Taking the Fourier transform of the yellow region indicated in Fig. 6(g), double electron diffraction spots were observed in Fig. 6(j), indicating that the Nb- and Zr-enriched nano-spherical precipitates containing stacking faults are linked to the matrix; a similar result was also reported for the $\text{Pb}_{0.935}\text{Cd}_{0.04}\text{Na}_{0.025}\text{Se}_{0.5}\text{S}_{0.25}\text{Te}_{0.25}$ high-entropy alloy [11]. This result was mainly attributed to the existent stress field fluctuations in the Nb- and Zr-enriched precipitates, as confirmed by the GPA results presented in Fig. 6(h) and (i). These stacking faults can also provide strong scattering for heat-carrying phonons in the $\text{Zr}_{0.6}(\text{NbTa})_{0.4}\text{CoSb}$ medium-entropy HH alloy. Compared with the

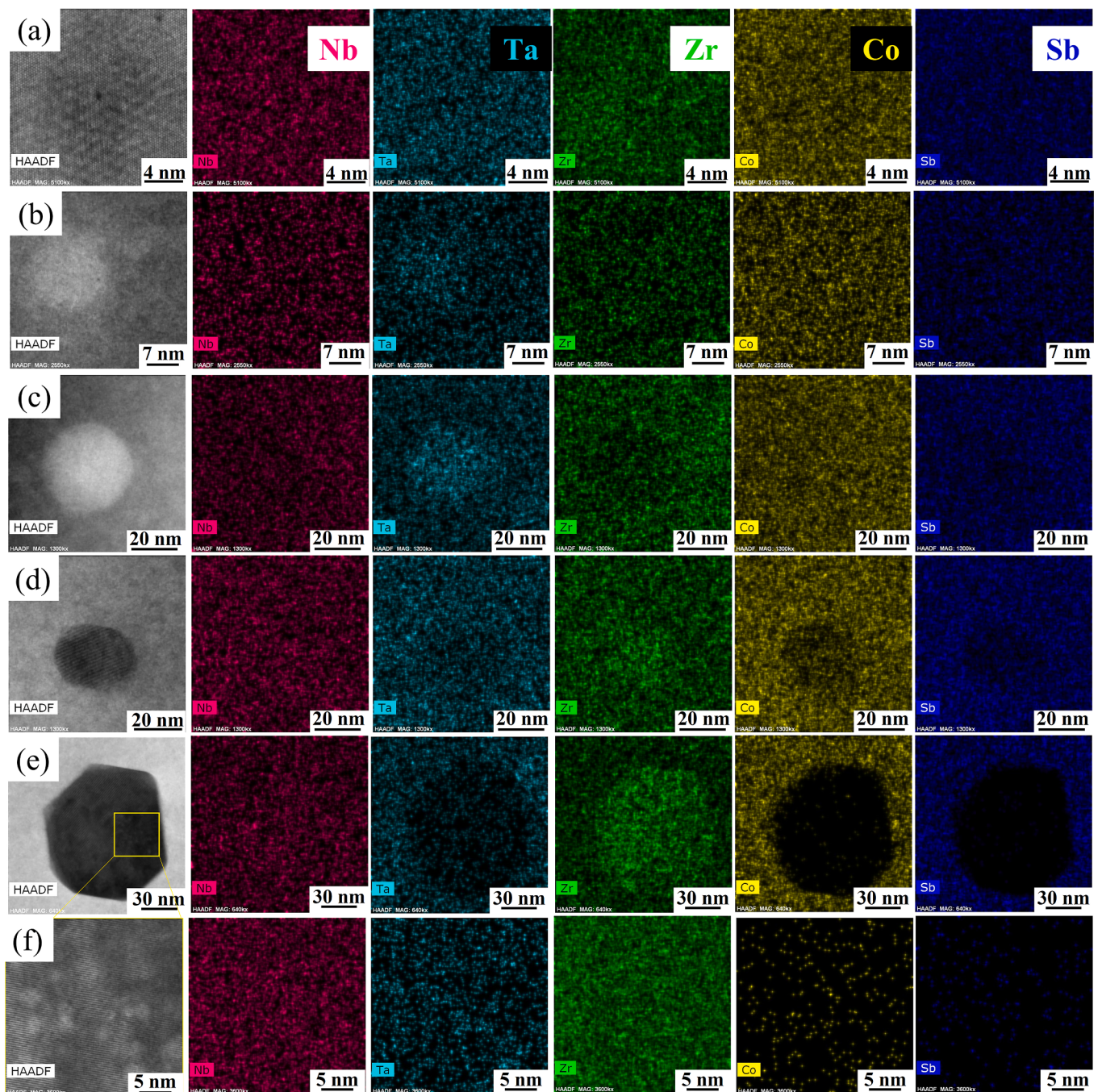


Fig. 5. HAADF-STEM images of typical nano-precipitates and their corresponding elemental mapping images for the Zr_{0.6}(NbTa)_{0.4}CoSb HH alloy: (a) Nb-enriched nano-domains; (b) and (c) Ta-enriched nano-precipitates; (d) Nb- and Zr-enriched nano-spherical precipitates; (e) Nb- and Ta-enriched nano-hexagonal precipitates; (f) Ta-enriched nano-domains in the area indicated by the yellow box in part (e). (For interpretation of the references to colour in this figure legend, the reader is referred to the web version of this article.)

single-doped counterpart, the Nb- and Zr-enriched nano-spherical precipitates containing stacking faults should be a specific source of phonon scattering in medium-entropy HHs.

3.4.2. Atomic disorder, sound velocities, and other physical parameters

To further shed light on the origin of ultralow κ_L , the sound velocities of HHs were measured. The longitudinal v_L , transverse v_T velocities, estimated values of the Debye temperature θ_D , Poisson ratio ν_p , and Grüneisen parameter γ for the Zr_{1-x}(NbTa)_xCoSb HHs were determined and are displayed in Table 1. Subsequently, the mean sound velocity v_m was derived from v_L and v_T using Eq. (2) [46]:

$$v_m = \left[\frac{1}{3} \left(\frac{1}{v_L^3} + \frac{2}{v_T^3} \right) \right]^{-1/3} \quad (2)$$

It should be noted here that the disorder scattering parameter Γ characterizes the point defect scattering, wherein a larger value of Γ indicates an enhanced scattering of phonons from point defects, as outlined in Eqs. (3)–(7) [47]:

$$\Gamma = \Gamma_M + \Gamma_S \quad (3)$$

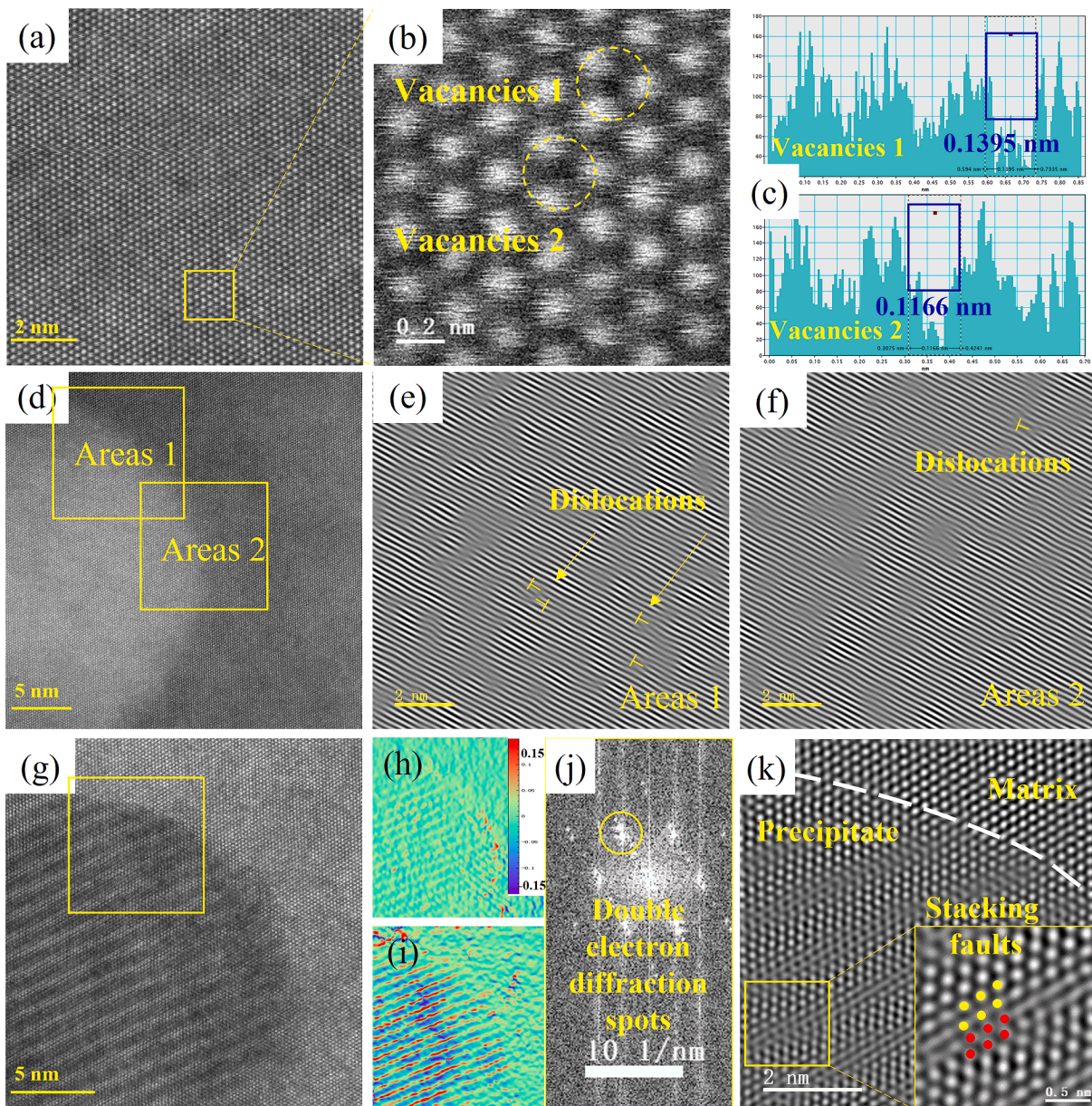


Fig. 6. Atomic structure of the $\text{Zr}_{0.6}(\text{NbTa})_{0.4}\text{CoSb}$ HH alloy: (a)–(c) vacancies, (d)–(f) dislocations, and (g) phase interfaces. GPA results along the (h) ε_{xx} and (i) ε_{yy} directions. (j) Electron diffraction spots, and (k) stacking faults.

Table 1

Sound velocities and calculated parameters for the $\text{Zr}_{1-x}(\text{NbTa})_x\text{CoSb}$ HHs at room temperature.

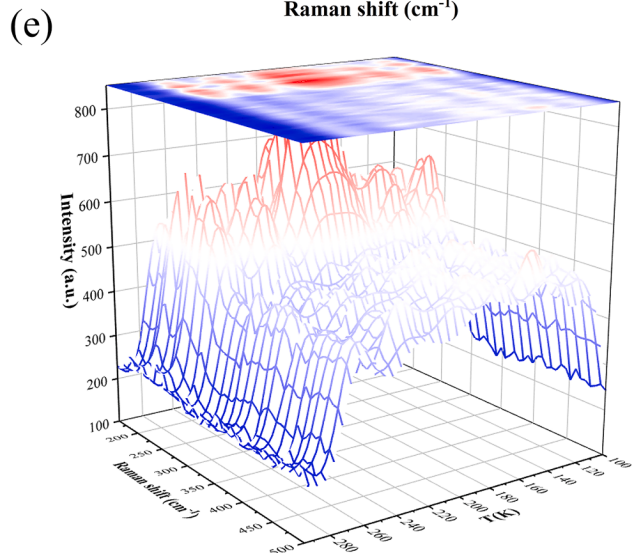
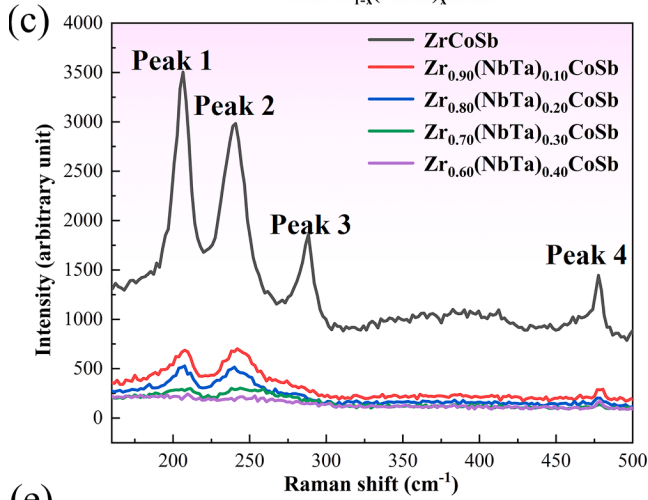
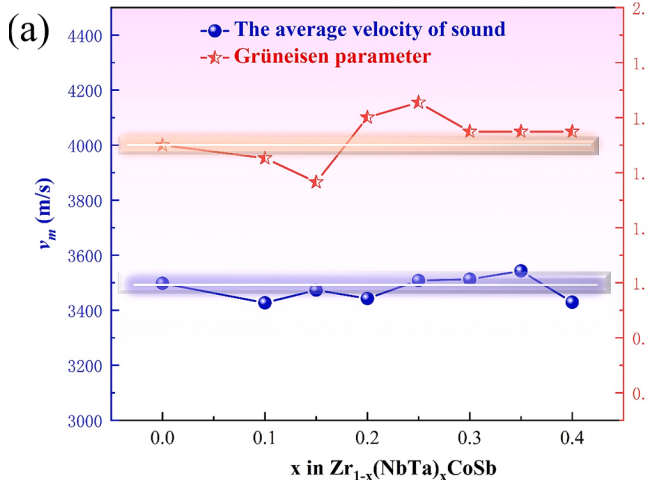
x	v_L (m/s)	v_T (m/s)	v_m (m/s)	θ_D (K)	γ	l_{ph} (nm)	v_p	ε
0	5479.45	3149.61	3498.01	383.7	1.51	42.5	0.25	–
0.10	5280.01	3090.73	3427.07	376.2	1.45	35.8	0.24	51.2
0.15	5245.9	3139.05	3473.46	392.5	1.37	27.2	0.22	41.5
0.20	5524.79	3092.82	3442.55	394.2	1.60	26.5	0.27	70.6
0.25	5740.46	3146.44	3508.02	406.3	1.66	23.9	0.28	78.8
0.30	5527.27	3161.60	3512.81	409.7	1.55	17.9	0.26	63.3
0.35	5562.79	3189.33	3542.91	416.0	1.55	17.3	0.26	63.3
0.40	5438.11	3084.03	3429.11	403.7	1.55	17.4	0.26	63.3

$$\Gamma_M = \frac{\sum_{i=1}^n c_i \left(\frac{M_i}{M}\right)^2 \Gamma_M^i}{\left(\sum_{i=1}^n c_i\right)} \quad (4)$$

$$\Gamma_M^i = \sum_k f_i^k \left(1 - \frac{M_i^k}{M_j}\right)^2 \quad (5)$$

$$\Gamma_s = \frac{\sum_{i=1}^n c_i \left(\frac{M_i}{M}\right)^2 f_i^1 f_i^2 \epsilon_i \left(\frac{r_i^1 - r_i^2}{\bar{r}_i}\right)^2}{\left(\sum_{i=1}^n c_i\right)} \quad (6)$$

$$\epsilon = \frac{2}{9} \left(\frac{6.4 \times \gamma (1 + \nu_p)}{1 - \nu_p} \right)^2 \quad (7)$$



where the disorder scattering parameters Γ_M and Γ_S are the mass and strain field fluctuations, respectively. The ϵ is a phenomenologically adjustable parameter that normally ranges from 10 to 100 [48]. The θ_D can be estimated from v_m using Eq. (8), where h is Planck's constant, and V is the unit cell volume:

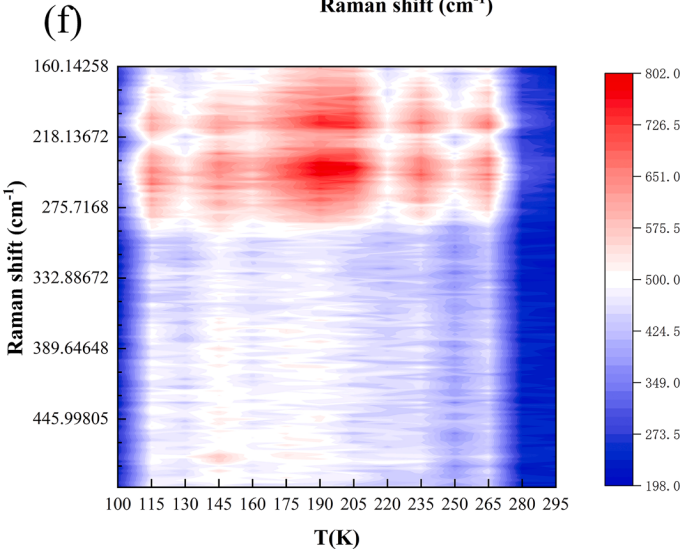
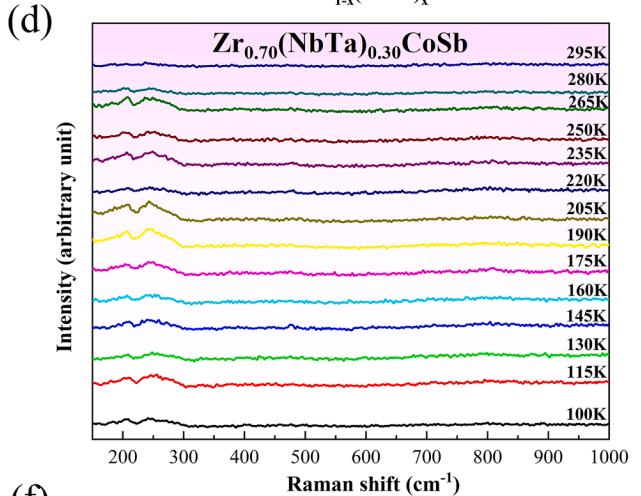
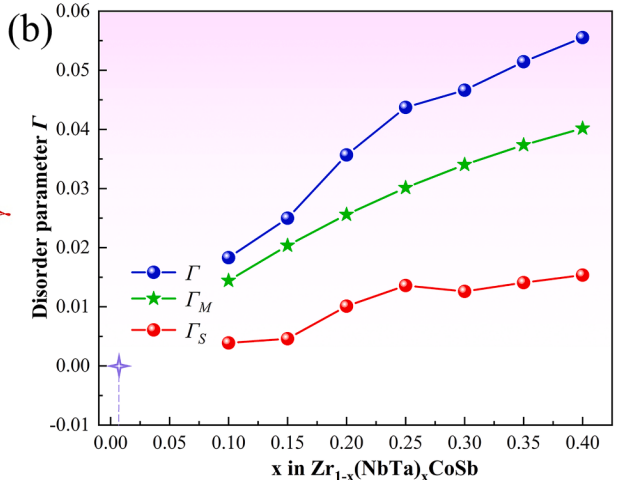


Fig. 7. Relationship between the degree of doping and the resulting values of (a) v_m and γ , and (b) the disorder parameters Γ . (c) Raman spectra of the $Zr_{1-x}(NbTa)_xCoSb$ ($x = 0, 0.1, 0.2, 0.3$, and 0.4) HHs at 300 K. (d) in situ Raman spectra of the $Zr_{0.70}(NbTa)_{0.30}CoSb$ HH alloy at 100–295 K, and the corresponding (e) 3D and (f) 2D Raman intensity plots.

$$\theta_D = \frac{h}{k_B} \left[\frac{3N}{4\pi V} \right]^{1/3} v_m \quad (8)$$

The relationships between the sound velocity and the values of v_p and γ are then given by Eqs. (9) and (10), respectively:

$$v_p = \frac{1 - 2(v_T/v_L)^2}{2 - 2(v_T/v_L)^2} \quad (9)$$

$$\gamma = \frac{3}{2} \left(\frac{1 + v_p}{2 - 3v_p} \right) \quad (10)$$

As shown in Fig. 7(a), the increasing entropy has no appreciable effect on v_m , while γ increases slightly overall, thereby indicating a stronger bond anharmonicity in the medium-entropy HHs. Fig. 7(b) confirms that the increasing mass and stress field fluctuations primarily contributed to the reduction in κ_L ; a similar finding was also reported by Hu et al. for a Zr_{0.5}Hf_{0.5}CoSb_{0.8}Sn_{0.2} HH alloy [46]. To further understand the extremely low κ_L obtained herein, the phonon mean free path l_{ph} for the HHs at room temperature was calculated using Eq. (11) [49],

$$\kappa_L = \frac{1}{3} d C_p v_m l_{ph} \quad (11)$$

where d denotes the density of the sample. As shown in Table 1, the calculated l_{ph} values of 17.4–35.8 nm for the Zr_{1-x}(NbTa)_xCoSb HHs are lower than that of the pristine ZrCoSb (42.5 nm), thereby indicating the presence of severe lattice distortions in the medium-entropy HHs, effectively reducing the l_{ph} and κ_L values, and confirming the key role of entropy engineering in controlling the κ_L of HH alloys. In addition, θ_D displays a slight overall increase, indicating the presence of an enhanced interatomic binding force, which is broadly in line with the calculated lattice constants shown in Fig. 1(b).

Fig. 7(c) shows the Raman spectra of the ZrCoSb-based HHs, wherein four characteristic Raman peaks are indexed. Upon increasing the configurational entropy, the half-height widths of peaks 1–3 gradually widened and finally disappeared, while peak 4 remained for the Zr_{1-x}(NbTa)_xCoSb HH alloy. This result indicates that the entropy-driven Zr-site disorder strengthens the phonon scattering. Fig. 7(d)–(f) show the temperature-dependent Raman spectra measured from 100 to

295 K for the Zr_{0.7}(NbTa)_{0.3}CoSb HH alloy. As shown in Fig. 7(d), upon increasing the temperature above 220 K, the half-height width of the Raman peaks gradually increased with the increasing entropy, indicating that the degree of disorder also concomitantly increased at temperatures > 220 K. To further elucidate the phonon scattering in the medium-entropy HHs, 3D and 2D temperature-dependent Raman intensity plots were analyzed for the Zr_{0.7}(NbTa)_{0.3}CoSb HH alloys, as shown in Fig. 8(e) and 8(f). Based on the obtained spectra, it was apparent that the degree of order became weaker in HHs at ~220 K, indicating that the long-range order of Zr-Co-Sb bonding begins to be disrupted. A similar result, in which the Raman peak attributed to the Bi-Se chain disappears due to the cation disordering at high temperatures, has also been reported for the (AgBiSe₂)_{0.7}(SnSe)_{0.3} alloy [50]. Moreover, the Raman spectra also confirm that disorder is promoted above room temperature, which is in agreement with the observed Co-interstitial defects shown in Fig. 6(b).

As shown in Fig. 8(a) and (b), as a gene-like performance indicator, the increasing entropy in a TE material leads to the existence of numerous lattice defects that provide extra point defects for scattering phonons and thereby suppress κ_L [35,36,51–58]. In particular, for the ZrCoSb-based medium-entropy HHs described herein, the presence of such vacancies, dislocations, nano-precipitates, and strong mass and strain field fluctuations in the Zr_{0.60}(NbTa)_{0.40}CoSb medium-entropy HH alloy significantly depresses the κ_L . Based on the results presented in Fig. 8(a) and (b), it is clear that increasing configurational entropy leads to a large suppression in κ_L , which was gradually closer to the theoretical limit at the high temperature range. A schematic representation of the phonon scattering mechanism for the medium-entropy HHs is presented in Fig. 8(c), which shows the phonons of all-scale hierarchical wavelengths scattered by various defects, and aids in understanding the role of highly-configurational entropy in the designed medium-entropy HHs. Moreover, through the synergy of entropy-driven multiscale microstructures (e.g., atomic disorder, vacancies, stacking faults, dislocations, nano-domain/precipitates, and electron-phonon interactions) following doping, an ultralow κ_L is achieved for the Zr_{0.60}NbTa_{0.40}CoSb HH alloy over the entire temperature range examined herein.

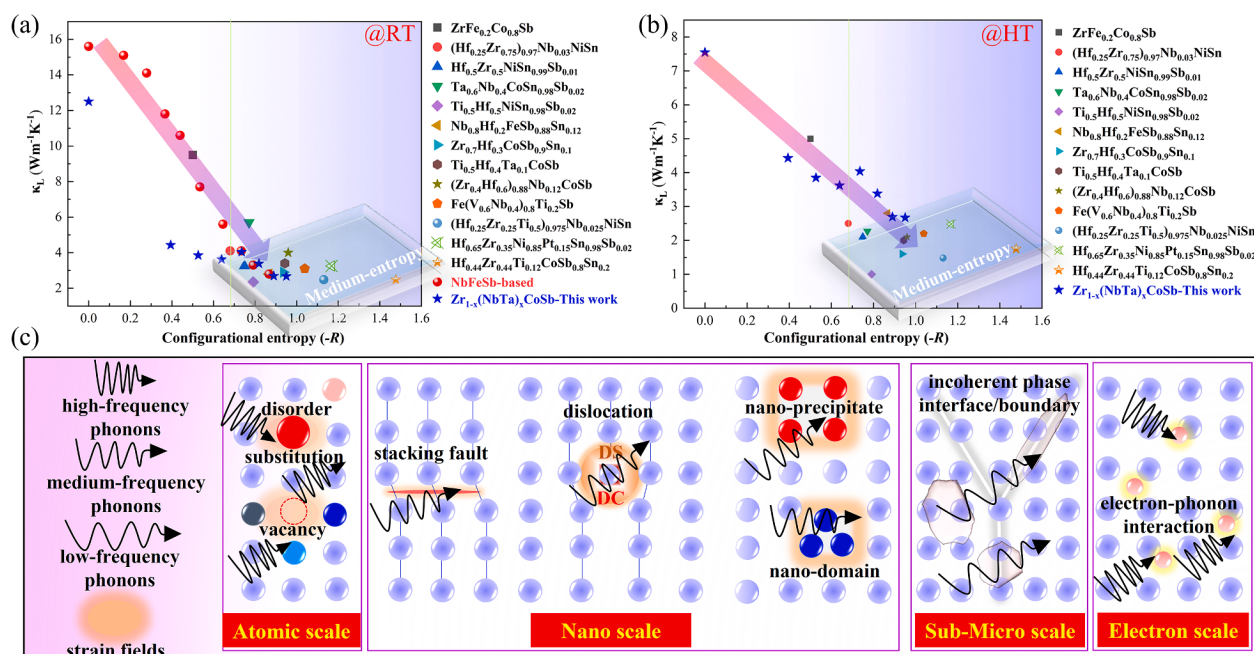


Fig. 8. Variation in κ_L as a function of the configurational entropy at (a) room temperature (RT) and (b) high temperature (HT) [35,36,51–58]. (c) Phonon scattering mechanism for the medium-entropy HHs.

3.5. Optimization of the sintering temperature

To further enhance the TE properties of HHs, the sintering temperature of the $Zr_{0.6}NbTa_{0.4}CoSb$ HH alloy with an ultralow κ_L was optimized. As shown in Fig. 9(a), upon increasing the sintering temperature from 1123 to 1323 K, σ was initially enhanced prior to reaching a plateau. In addition, it is evident from Fig. 9(b) that the absolute value

of S decreases and then increases upon increasing the sintering temperature. Benefiting from the enhanced σ , PF_{\max} was improved by 40.2 %, reaching $1.5 \times 10^{-3} \text{ W cm}^{-1} \text{ K}^{-2}$ at 923 K for the sample sintered at 1323 K. As shown in Fig. 9(c), the κ of all samples are higher than that of the sample sintered at 1123 K, with the exception of the sample sintered at 1273 K. Fig. 9(d) shows the sintering temperature-dependent ZT, wherein the highest ZT_{\max} value of ~ 0.42 was achieved for

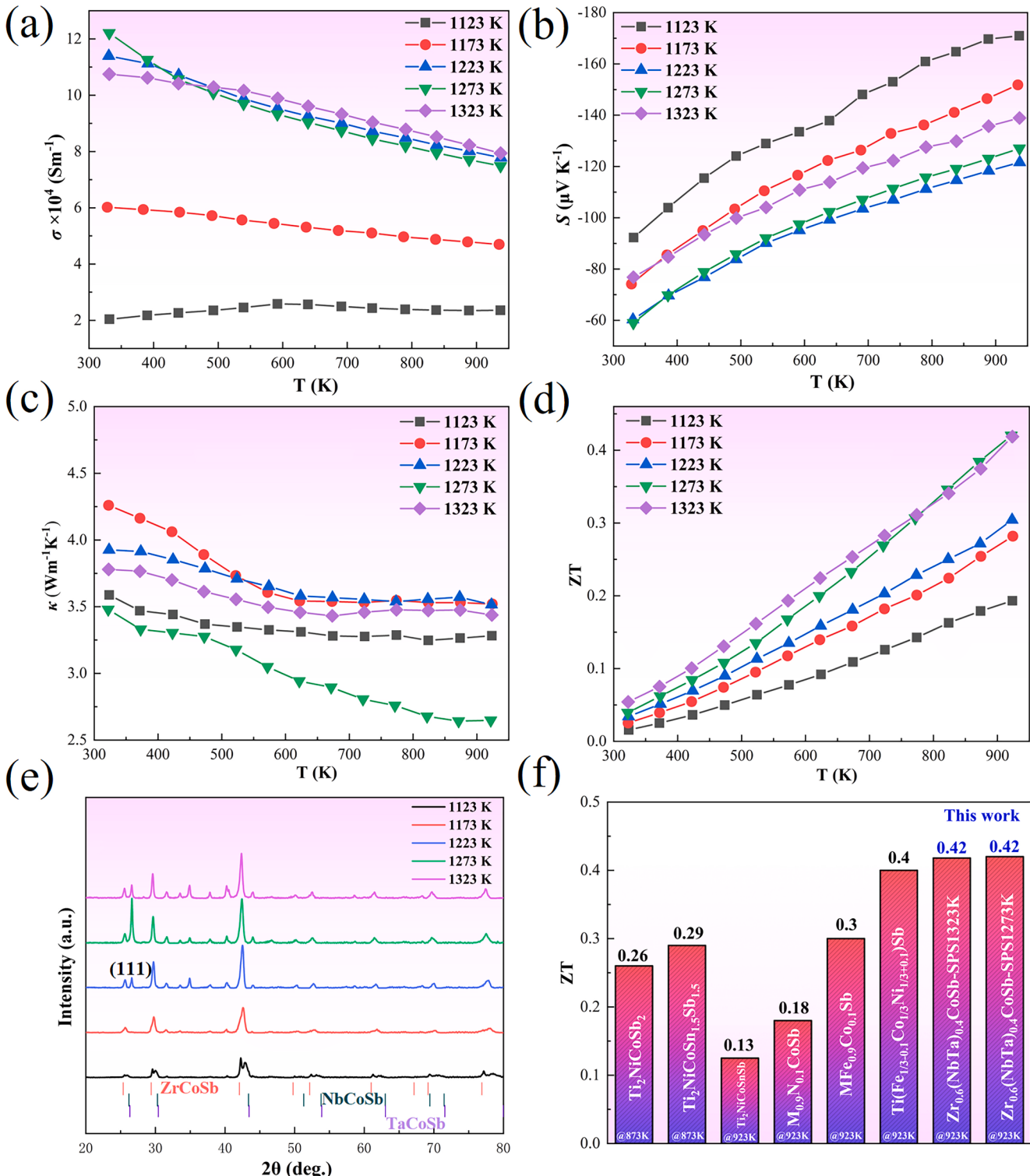


Fig. 9. Effects of the sintering temperature on the values of (a) σ , (b) S , (c) κ , and (d) ZT for $Zr_{0.6}(NbTa)_0.4CoSb$ HH alloy. (e) XRD patterns of the samples obtained at a range of sintering temperatures. (f) ZT_{\max} values of various MCoSb-based HHs obtained by entropy engineering.

$Zr_{0.60}(NbTa)_{0.40}CoSb$ at 923 K (sintered at 1273 K). Significantly, as shown in the XRD patterns presented in Fig. 9(e), an increase in the sintering temperature resulted in a gradual disappearance of the split peaks, although negligible precipitates were detected. When the sintering temperature was increased > 1123 K, the (111) peaks of Nb/TaCoSb and ZrCoSb began to coexist, and the strongest diffraction intensity was present in the sample sintered at 1273 K. Therefore, it is reasonable to infer that the synergistic effect of texture and precipitates plays a key role in decreasing the κ_L [59,60], although the enhancement in σ resulting in electron–phonon interactions also should be considered. Thus, the corresponding phonon transport mechanisms resulting from optimization of the sintering temperature must be further evaluated in future studies. Finally, as shown in Fig. 9(f), the optimized ZT_{max} is comparable or even superior to those of other medium- and high-entropy MCoSb-based HHs. This work therefore illustrates that the design of Zr-sites with high configurational entropies, in addition to optimization of the sintering temperature, are highly effective for decreasing the κ_L and enhancing the TE properties of MCoSb-based HHs.

4. Conclusions

In the context of entropy engineering, we manipulated the Zr-site configurational entropy to attain a delicate balance between the structural order (i.e., MgAgAs structure) and disorder (i.e., the medium-entropy of mixing and multiscale defects) in ZrCoSb-based HHs. Benefiting from the co-doping of Nb and Ta donors, an optimized maximum power factor (PF_{max}) of $1.8 \times 10^{-3} \text{ W m}^{-1} \text{ K}^{-2}$ was achieved in the $Zr_{0.80}(NbTa)_{0.20}CoSb$ HH alloy at 923 K. In addition, the lattice thermal conductivity (κ_L) reduced from $7.5 \text{ W K}^{-1} \text{ m}^{-1}$ for the pristine alloy to $2.8 \text{ W K}^{-1} \text{ m}^{-1}$ for the $Zr_{0.6}(NbTa)_{0.4}CoSb$ HH alloy at 923 K.

Following a comprehensive evaluation of the electrical and thermal properties, a peak dimensionless figure-of-merit (ZT) of ~ 0.35 was obtained for the $Zr_{0.8}(NbTa)_{0.2}CoSb$ HH alloy sintered at 1173 K. Furthermore, using the $Zr_{0.6}(NbTa)_{0.4}CoSb$ HH alloy as the reference alloy, the sintering temperature was optimized to enhance its electrical properties, and the highest ZT of ~ 0.42 was achieved for the $Zr_{0.6}(NbTa)_{0.4}CoSb$ alloy sintered at 1273 K.

Density functional theory calculations indicated that a poor Seebeck coefficient was induced by a lower density-of-states (DOS) effective mass and a slowly changing DOS at Fermi level, which are considered to be the main factors responsible for hindering the further development of medium-entropy HHs. The exciting microstructures, including stacking faults in Nb- and Ta-enriched precipitates and Ta-enriched nano-domains, have been observed in ZrCoSb-based medium-entropy HHs. Due to the entropy-driven synergy of multiscale microstructures, such as the atomic disorder, vacancies, stacking faults, dislocations, nano-domains/precipitates, and electron–phonon interactions, the lowest κ_L of $1.27 \text{ W m}^{-1} \text{ K}^{-1}$ was achieved for the $Zr_{0.6}(NbTa)_{0.4}CoSb$ alloy at 923 K (sintered at 1173 K), which is $\sim 82.9\%$ lower than that of the pristine ZrCoSb HH alloy. Moreover, the disorder scattering parameters and the geometric phase analysis indicate that the increasing mass and stress field fluctuations also play a key role in reducing κ_L .

In situ Raman spectroscopy confirmed that atomic disordering is promoted upon increasing the temperature above 220 K, which is in agreement with the observed Co-interstitial defects. The multiscale defects present in the medium-entropy HHs were also demonstrated to effectively reduce the phonon mean free path, which provides a potential means to further reduce κ_L . Overall, this work provides guidance for the design of medium-entropy HHs to achieve an excellent Seebeck coefficient and thermoelectric properties, and we anticipate that our results will motivate broader research on entropy engineering to prepare state-of-art HHs.

Declaration of Competing Interest

The authors declare that they have no known competing financial

interests or personal relationships that could have appeared to influence the work reported in this paper.

Data availability

Data will be made available on request.

Acknowledgements

This work was financially supported by the National Natural Science Foundation of China (Grant Nos. 52271025, 51971052, 51927801, and 51834009), the Liaoning Revitalization Talents Program (No. XLYC2007183), and the Innovation Foundation of Science and Technology of Dalian (Nos. 2020JJ25CY002 and 2020JJ26GX045).

References

- [1] T. Zhu, L. Hu, X. Zhao, J. He, New Insights into Intrinsic Point Defects in V_2V_{13} Thermoelectric Materials, *Adv. Sci.* 3 (7) (2016) 1600004, <https://doi.org/10.1002/advs.201600004>.
- [2] W. Li, S. Lin, B. Ge, J. Yang, W. Zhang, Y. Pei, Low Sound Velocity Contributing to the High Thermoelectric Performance of Ag_8SnSe_6 , *Adv. Sci.* 3 (11) (2016) 1600196, <https://doi.org/10.1002/advs.201600196>.
- [3] W. Zeier, J. Schmitt, G. Hautier, U. Aydemir, Z. Gibbs, C. Felser, G. Snyder, Engineering half-Heusler thermoelectric materials using Zintl chemistry, *Nat. Rev. Mater.* 1 (6) (2016) 16032, <https://doi.org/10.1038/natrevmats.2016.32>.
- [4] H. Zhu, J. Mao, Y. Li, J. Sun, Y. Wang, Q. Zhu, G. Li, Q. Song, J. Zhou, Y. Fu, R. He, T. Tong, Z. Liu, W. Ren, L. You, Z. Wang, J. Luo, A. Sotnikov, J. Bao, K. Nielsch, G. Chen, D. Singh, Z. Ren, Discovery of $TaFeSb$ -based half-Heuslers with high thermoelectric performance, *Nat. Commun.* 10 (1) (2019) 270, <https://doi.org/10.1038/s41398-018-0223-5>.
- [5] C. Fu, S. Bai, Y. Liu, Y. Tang, L. Chen, X. Zhao, T. Zhu, Realizing high figure of merit in heavy-band p-type half-Heusler thermoelectric materials, *Nat. Commun.* 6 (1) (2015) 8144, <https://doi.org/10.1038/ncomms9144>.
- [6] H.A. Rahnamaye Aliabad, Z. Nodehi, B. Maleki, A. Abarehi, Electronical and thermoelectric properties of half-Heusler $ZrNiPb$ under pressure in bulk and nanosheet structures for energy conversion, *Rare Met.* 38 (11) (2019) 1015–1023.
- [7] H. Zhu, R. He, J. Mao, Q. Zhu, C. Li, J. Sun, W. Ren, Y. Wang, Z. Liu, Z. Tang, A. Sotnikov, Z. Wang, D. Broido, D.J. Singh, G. Chen, K. Nielsch, Z. Ren, Discovery of $ZrCoBi$ based half Heuslers with high thermoelectric conversion efficiency, *Nat. Commun.* 9 (1) (2018) 2497, <https://doi.org/10.1038/s41398-018-04958-3>.
- [8] X. Yan, G. Joshi, W. Liu, Y. Lan, H. Wang, S. Lee, J.W. Simonson, S.J. Poon, T. M. Tritt, G. Chen, Z.F. Ren, Enhanced thermoelectric figure of merit of p-type half-Heuslers, *Nano Lett.* 11 (2) (2011) 556–560, <https://doi.org/10.1021/nl104138t>.
- [9] R. Quinn, J. Bos, Advances in half-Heusler alloys for thermoelectric power generation, *Mater. Adv.* 2 (2021) 6246–6266, <https://doi.org/10.1039/dima00707f>.
- [10] H. Jeong, S.K. Kihoi, J.N. Kahiu, H. Kim, J. Ryu, K.H. Lee, S. Yi, H.S. Lee, Origin of low thermal conductivity in $Nb_{1-x}Ti_xFe_{1.02}Sb$ half-Heusler thermoelectric materials, *J. Eur. Ceram. Soc.* 41 (7) (2021) 4175–4181.
- [11] B. Jiang, Y. Yu, H. Chen, J. Cui, X. Liu, L. Xie, J. He, Entropy engineering promotes thermoelectric performance in p-type chalcogenides, *Nat. Commun.* 12 (1) (2021) 3234, <https://doi.org/10.1038/s41467-021-23569-z>.
- [12] B. Jiang, W. Wang, S. Liu, Y. Wang, C. Wang, Y. Chen, L. Xie, M. Huang, J. He, High figure-of-merit and power generation in high-entropy $GeTe$ -based thermoelectrics, *Science* 377 (2022) 208–213, <https://doi.org/10.1126/science.abq5815>.
- [13] B. Jiang, Y. Yu, J. Cui, X. Liu, L. Xie, J. Liao, Q. Zhang, Y. Huang, S. Ning, B. Jia, B. Zhu, S. Bai, L. Chen, S.J. Pennycook, J. He, High-entropy-stabilized chalcogenides with high thermoelectric performance, *Science* 371 (2021) 830–834, <https://doi.org/10.1126/science.abe1292>.
- [14] S. Roychowdhury, T. Ghosh, R. Arora, U. Waghmare, K. Biswas, Stabilizing n-type cubic $GeSe$ by entropy-driven alloying of $AgBiSe_2$: Ultralow thermal conductivity and promising thermoelectric performance, *Angew. Chem. Int. Ed. Engl.* 57 (2018) 15167–15171, <https://doi.org/10.1002/anie.201809841>.
- [15] C. Liu, Y. Yang, Z. Zhou, C. Nan, Y. Lin, $(Ti_{0.2}V_{0.2}Cr_{0.2}Nb_{0.2}Ta_{0.2})_2AlC - (Ti_{0.2}V_{0.2}Cr_{0.2}Nb_{0.2}Ta_{0.2})_2C$ high-entropy ceramics with low thermal conductivity, *J. Am. Ceram. Soc.* 103 (2021) 2744–2771, <https://doi.org/10.1111/jace.18252>.
- [16] P. Zhang, Z. Lou, M. Qin, J. Xu, J. Zhu, Z. Shi, Q. Chen, M.J. Reece, H. Yan, F. Gao, High-entropy $(Ca_{0.2}Sr_{0.2}Ba_{0.2}La_{0.2}Pb_{0.2})TiO_3$ perovskite ceramics with A-site short-range disorder for thermoelectric applications, *J. Mater. Sci. Technol.* 97 (2022) 182–189.
- [17] X. Wang, H. Yao, Z. Zhang, X. Li, C. Chen, L.i. Yin, K. Hu, Y. Yan, Z. Li, B.o. Yu, F. Cao, X. Liu, X.i. Lin, Q. Zhang, Enhanced Thermoelectric Performance in High Entropy Alloys $Sn_{0.25}Pb_{0.25}Mn_{0.25}Ge_{0.25}Te$, *ACS Appl. Mater. Interfaces* 13 (16) (2021) 18638–18647.
- [18] Y. Wu, X. Su, D. Yang, Q. Zhang, X. Tang, Boosting thermoelectric properties of $AgBi_3(Se_yS_{1-y})_5$ solid solution via entropy engineering, *ACS Appl. Mater. Interfaces* 13 (3) (2021) 4185–4191, <https://doi.org/10.1021/acsami.0c19387>.
- [19] Y. Wang, B. Qin, T. Hong, L. Su, X. Gao, D. Wang, L. Zhao, Enhanced thermoelectric performance in cubic form of $SnSe$ stabilized through enformatively

- alloying AgSbTe₂, *Acta Mater.* 227 (2022), 117681, <https://doi.org/10.1016/j.actamat.2022.117681>.
- [20] T. Zhao, H. Zhu, B. Zhang, S. Zheng, N. Li, G. Wang, G. Wang, X. Lu, X. Zhou, High thermoelectric performance of tellurium-free n-type AgBi_{1-x}Sb_xSe₂ with stable cubic structure enabled by entropy engineering, *Acta Mater.* 220 (2021), 117291, <https://doi.org/10.1016/j.actamat.2021.117291>.
- [21] J. Yan, F. Liu, G. Ma, B. Gong, J. Zhu, X. Wang, W. Ao, C. Zhang, Y. Li, J. Li, Suppression of the lattice thermal conductivity in NbFeSb-based half-Heusler thermoelectric materials through high entropy effects, *Scr. Mater.* 157 (2018) 129–134, <https://doi.org/10.1016/j.scriptamat.2018.08.008>.
- [22] K. Chen, R. Zhang, J. Bos, M. Reece, Synthesis and thermoelectric properties of high-entropy half-Heusler MFe_{1-x}Co_xSb (M = equimolar Ti, Zr, Hf, V, Nb, Ta), *J. Alloy. Compd.* 892 (2022), 162045, <https://doi.org/10.1016/j.jallcom.2021.162045>.
- [23] A. Karati, S. Mishra, S. Ghosh, R. Mallik, R. Shabadi, R. Ramanujan, S. Yadav, B. Murty, U. Varadaraju, Thermoelectric properties of a high entropy half-Heusler alloy processed by a fast powder metallurgy route, *J. Alloys Compd.* 924 (2022), 166108, <https://doi.org/10.1016/j.jallcom.2022.166108>.
- [24] G. Kresse, J. Furthmüller, Efficiency of Ab-initio total energy calculations for metals and semiconductors using a plane-wave basis set, *Comput. Mat. Sci.* 6 (1) (1996) 15–50, [https://doi.org/10.1016/0927-0256\(96\)00008-0](https://doi.org/10.1016/0927-0256(96)00008-0).
- [25] G. Kresse, J. Furthmüller, Efficient iterative schemes for ab initio total-energy calculations using a plane-wave basis set, *Phys. Rev. B* 54 (16) (1996) 11169–11186, <https://doi.org/10.1103/physrevb.54.11169>.
- [26] P. Blöchl, Projector augmented-wave method, *Phys. Rev. B* 50 (24) (1994) 17953–17979.
- [27] J. Perdew, K. Burke, M. Ernzerhof, Generalized gradient approximation made simple, *Phys. Rev. Lett.* 77 (18) (1996) 3865–3868, <https://doi.org/10.1103/physrevlett.77.3865>.
- [28] M. Chen, M. Weinert, Layer k-projection for unfolding electronic bands of interfaces, *Phys. Rev. B* 98 (24) (2018), 245421, <https://doi.org/10.1103/physrevb.98.245421>.
- [29] M. Chen, W. Chen, Z. Zhang, M. Weinert, Effects of magnetic dopants in (Li_{0.8}Mg_{0.2}O)₂FeSe (M=Fe, Mn, Co): Density functional theory study using a band unfolding technique, *Phys. Rev. B* 96 (24) (2017), 245111, <https://doi.org/10.1103/PhysRevB.96.245111>.
- [30] M. Chen, M. Weinert, Revealing the substrate origin of the linear dispersion of silicene/Ag(111), *Nano Lett.* 14 (9) (2014) 5189–5193, <https://doi.org/10.1021/nl502107v>.
- [31] N. Lu, L. Li, M. Liu, A review of carrier thermoelectric-transport theory in organic semiconductors, *PCCP* 18 (29) (2016) 19503–19525, <https://doi.org/10.1039/c6cp02830f>.
- [32] R. Min, Y. Wang, X. Jiang, R. Chen, H. Kang, E. Guo, Z. Chen, X. Yang, T. Wang, Significantly improved thermoelectric properties of Nb-doped ZrNiSn half-Heusler compounds, *Chem. Eng. J.* 449 (2022), 137898, <https://doi.org/10.1016/j.cej.2022.137898>.
- [33] C. Fu, T. Zhu, Y. Liu, H. Xie, X. Zhao, Band engineering of high performance p-type FeNbSb based half-Heusler thermoelectric materials for figure of merit zT > 1, *Energ. Environ. Sci.* 8 (1) (2015) 216–220, <https://doi.org/10.1039/c4ee03042g>.
- [34] A. El-Khouly, A. Novitskii, I. Serhiienko, A. Kalugina, A. Sedegov, D. Karpenkov, A. Voronin, V. Khovaylo, A. Adam, Optimizing the thermoelectric performance of FeVsB half-Heusler compound via Hf-Ti double doping, *J. Power Sources* 477 (30) (2020), 228768, <https://doi.org/10.1016/j.jpowsour.2020.228768>.
- [35] M.A.A. Mohamed, E.M.M. Ibrahim, N.P. Rodriguez, S. Hampel, B. Büchner, G. Schiering, K. Nielsch, R. He, Tuning of the electronic and phononic properties of NbFeSb half-Heusler compound by Sn/Hf co-doping, *Acta Mater.* 196 (2020) 669–676.
- [36] C. Hsu, H. Ma, Microstructure and thermoelectric properties in Fe-doped ZrCoSb half-Heusler compound, *Mater. Sci. Eng. B* 198 (2015) 80–85, <https://doi.org/10.1016/j.mseb.2015.03.015>.
- [37] Y. Liu, J. Makongo, A. Page, P. Sahoo, C. Uher, K. Stokes, P. Poudeau, Distribution of impurity states and charge transport in Zr_{0.25}Hf_{0.75}Ni_{1+x}Sn_{1-x}Sb nanocomposites, *J. Solid State Chem.* 234 (2016) 72–86, <https://doi.org/10.1016/j.jssc.2015.11.035>.
- [38] W. Xie, Y. Yan, S. Zhu, M. Zhou, S. Populoh, K. Galazka, S. Poon, A. Weidenkaff, J. He, X. Tang, T. Tritt, Significant ZT enhancement in p-type Ti(Co, Fe)Sb–InSb nanocomposites via a synergistic high-mobility electron injection, energy-filtering and boundary-scattering approach, *Acta Mater.* 61 (2013) 2087–2094, <https://doi.org/10.1016/j.actamat.2012.12.028>.
- [39] P. Luo, Y. Mao, Z. Li, J. Zhang, J. Luo, Entropy engineering: A simple route to both p- and n-type thermoelectrics from the same parent material, *Mater. Today. Phys.* 26 (2022), 100745, <https://doi.org/10.1016/j.mtphys.2022.100745>.
- [40] W. Ren, Q. Song, H. Zhu, J. Mao, L. You, G.A. Gamage, J. Zhou, T. Zhou, J. Jiang, C. Wang, J. Luo, J. Wu, Z. Wang, G. Chen, Z. Ren, Intermediate-level doping strategy to simultaneously optimize power factor and phonon thermal conductivity for improving thermoelectric figure of merit, *Mater. Today. Phys.* 15 (2020), 100250, <https://doi.org/10.1016/j.mtphys.2020.100250>.
- [41] J. Sootsman, D. Chung, M. Kanatzidis, New and old concepts in thermoelectric materials, *Angew. Chem. Int. Ed. Engl.* 48 (46) (2009) 8616–8639, <https://doi.org/10.1002/anie.200900598>.
- [42] K. Johari, D. Sharma, A. Verma, R. Bhardwaj, N. Chauhan, S. Kumar, M. Singh, S. Bathula, B. Gahtori, In situ evolution of secondary metallic phases in off-stoichiometric ZrNiSn for enhanced thermoelectric performance, *ACS Appl. Mater. Interfaces* 14 (2022) 19579–19593, <https://doi.org/10.1021/acsmi.2c03065>.
- [43] Q. Yang, T. Lyu, B. Nan, Y. Dong, J. Tie, G. Xu, Locally ordered nano-domains as novel microstructure defects suppressing the phonon transport in SnTe thermoelectrics, *J. Eur. Ceram. Soc.* 42 (3) (2022) 1001–1006, <https://doi.org/10.1016/j.jeurceramsoc.2021.11.022>.
- [44] X. Yang, Z. Jiang, J. Li, H. Kang, D. Liu, F. Yang, Z. Chen, E. Guo, X. Jiang, T. Wang, Identification of the intrinsic atomic disorder in ZrNiSn-based alloys and their effects on thermoelectric properties, *Nano Energy* 78 (2020), 105372, <https://doi.org/10.1016/j.nanoen.2020.105372>.
- [45] S. Yamini, D. Mitchell, Z. Gibbs, R. Santos, V. Patterson, S. Li, Y. Pei, S. Dou, G. Snyder, Heterogeneous distribution of sodium for high thermoelectric performance of p-type multiphase lead-chalcogenides, *Adv. Energy Mater.* 5 (21) (2015) 1501047, <https://doi.org/10.1002/aenm.201501047>.
- [46] C. Hu, K. Xia, X. Chen, X. Zhao, T. Zhu, Transport mechanisms and property optimization of p-type (Zr, Hf)CoSb half-Heusler thermoelectric materials, *Mater. Today. Phys.* 7 (2018) 69–76, <https://doi.org/10.1016/j.mtphys.2018.11.002>.
- [47] N. Kempf, C. Karthik, B.J. Jaques, J. Gigax, L. Shao, D.P. Butt, R. He, D. Wang, Z. Ren, Y. Zhang, Proton irradiation effect on thermoelectric properties of nanostructured n-type half-Heusler Hf_{0.25}Zr_{0.75}NiSn_{0.99}Sb_{0.01}, *Appl. Phys. Lett.* 112 (24) (2018) 243902.
- [48] C. Wan, W. Pan, Q. Xu, Y. Qin, J. Wang, Z. Qu, M. Fang, *Phys. Rev. B*. Effect of point defects on the thermal transport properties of (La_xGd_{1-x})₂Zr₂O₇: Experiment and theoretical model, 74(14) (2006) 144109. doi:10.1103/physrevb.74.144109.
- [49] Z. Chen, X. Zhang, Y. Pei, Manipulation of phonon transport in thermoelectrics, *Adv. Mater.* 30 (17) (2018) 1705617, <https://doi.org/10.1002/adma.201705617>.
- [50] H. Jang, M. Torigama, S. Abbey, B. Frimppong, J. Male, G. Snyder, Y. Jung, M. Oh, Suppressing charged cation antisites via Se vapor annealing enables p-type dopability in AgBiSe₂-SnSe thermoelectrics, *Adv. Mater.* 34 (38) (2022) 2204132, <https://doi.org/10.1002/adma.202204132>.
- [51] S. Li, H. Zhu, J. Mao, Z. Feng, X. Li, C. Chen, F. Cao, X. Liu, D. Singh, Z. Ren, Q. Zhang, N-type TaCoSn-based half-Heuslers as promising thermoelectric materials, *ACS Appl. Mater. Interfaces* 11 (2019) 41321–41329, <https://doi.org/10.1021/acsami.9b13603>.
- [52] H. Lee, K. Lee, L. Fu, G. Han, H. Kim, S. Kim, Y. Kim, S. Kim, Critical role of atomic-scale defect disorders for high-performance nanostructured half-Heusler thermoelectric alloys and their thermal stability, *Acta Mater.* 180 (2019) 97–104, <https://doi.org/10.1016/j.actamat.2019.09.004>.
- [53] H. Zhang, Y. Wang, K. Dahal, J. Mao, L. Huang, Q. Zhang, Z. Ren, Thermoelectric properties of n-type half-Heusler compounds (Hf_{0.25}Zr_{0.75})_{1-x}Nb_xNiSn, *Acta Mater.* 113 (2016) 41–47, <https://doi.org/10.1016/j.actamat.2016.04.039>.
- [54] Y. Liu, C. Fu, K. Xia, J. Yu, X. Zhao, H. Pan, C. Felser, T. Zhu, Lanthanide contraction as a design factor for high-performance half-Heusler thermoelectric materials, *Adv. Mater.* 30 (32) (2018) 1800881, <https://doi.org/10.1002/adma.201800881>.
- [55] C. Fu, C. Fu, K. Xia, H. Wang, G. Snyder, Y. Liu, Y. Liu, X. Zhao, High band degeneracy contributes to high thermoelectric performance in p-type half-Heusler compounds, *Adv. Energy Mater.* 4 (18) (2014) 1400600, <https://doi.org/10.1002/aenm.201400600>.
- [56] X. Yan, W. Liu, S. Chen, H. Wang, Q. Zhang, G. Chen, Z. Ren, Thermoelectric property study of nanostructured p-type half-Heuslers (Hf, Zr, Ti)CoSb_{0.8}Sn_{0.2}, *Adv. Energy Mater.* 3 (9) (2013) 1195–1200, <https://doi.org/10.1002/aenm.201200973>.
- [57] H. Xie, H. Wang, Y. Pei, H. Xie, H. Wang, G. Snyder, Y. Liu, Y. Liu, X. Zhao, High band degeneracy contributes to high thermoelectric performance in p-type half-Heusler compounds, *Adv. Energy Mater.* 4 (18) (2014) 1400600, <https://doi.org/10.1002/aenm.201400600>.
- [58] N. Chauhan, S. Bathula, A. Vishwakarma, R. Bhardwaj, K. Johari, B. Gahtori, A. Dhar, Enhanced thermoelectric performance in p-type ZrCoSb based half-Heusler alloys employing nanostructuring and compositional modulation, *J. Materiomics* 5 (1) (2019) 94–102, <https://doi.org/10.1016/j.jmat.2018.11.003>.
- [59] D. Bao, J. Chen, Y. Yu, W. Liu, L. Huang, G. Han, J. Tang, D. Zhou, L. Yang, Z. Chen, Texture-dependent thermoelectric properties of nano-structured Bi₂Te₃, *Chem. Eng. J.* 388 (15) (2020), 124295, <https://doi.org/10.1016/j.cej.2020.124295>.
- [60] P. Zhang, M. Qin, Z. Lou, S. Cao, L. Gong, J. Xu, M.J. Reece, H. Yan, Z. Dashevsky, F. Gao, Grain orientation evolution and multi-scale interfaces enhanced thermoelectric properties of textured Sr_{0.9}La_{0.1}TiO₃ based ceramics, *J. Eur. Ceram. Soc.* 42 (15) (2022) 7017–7026, <https://doi.org/10.1016/j.jeurceramsoc.2022.08.009>.